Bioorg. Med. Chem. 35 (2021) 116077

Contents lists available at ScienceDirect

Bioorganic & Medicinal Chemistry

journal homepage: www.elsevier.com/locate/bmc

Loop-mediated fluorescent probes for selective discrimination of parallel and antiparallel G-Quadruplexes

Anup Pandith [a], Upendra Nagarajachari [b], Ravi Kumara Guralamatta Siddappa [a], Sungjin Lee [c], Chin–Ju Park [c], Krishnaveni Sannathammegowda [b], Young Jun Seo [a,*]

[a] Department of Chemistry, Jeonbuk National University, Jeonju 54896, Republic of Korea
[b] Department of Physics, University of Mysore, Karnataka 570006, India
[c] Department of Chemistry, Gwangju Institute of Science and Technology, Gwangju 61005, Republic of Korea

ARTICLE INFO

Keywords:
G-Quadruplexes
Intramolecular charge transfer
Molecular confinements
Disaggregation
Molecular dynamics

ABSTRACT

Herein we report simple pyridinium (**1**–**3**) and quinolinium (**4**) salts for the selective recognition of G-quadruplexes (G4s). Among them, the probe **1**, interestingly, selectively discriminated parallel (c-KIT-1, c-KIT-2, c-MYC) G4s from anti-parallel/hybrid (22AG, HRAS-1, BOM-17, TBA) G4s at pH 7.2, through a switch on response in the far-red window. Significant changes in the absorption (broad 575 nm → sharp 505 nm) and emission of probe **1** at 620 nm, attributed to selective interaction with parallel G4s, resulted in complete disaggregation-induced monomer emission. Symmetrical push/pull molecular confinements across the styryl units in probe **1** enhanced the intramolecular charge transfer (ICT) by restricting the free rotation of C═C units in the presence of sterically less hindered and highly accessible G4 surface/bottom tetrads in the parallel G4s, which is relatively lower extent in antiparallel/hybrid G4s. We confirm that the disaggregation of probe **1** was very effective in the presence of parallel G4–forming ODNs, due to the presence of highly available free surface area, resulting in additional π-stacking interactions. The selective sensing capabilities of probe **1** were analyzed using UV–Vis spectroscopy, fluorescence spectroscopy, molecular dynamics (MD)–based simulation studies, and ^{1}H NMR spectroscopy. This study should afford insights for the future design of selective compounds targeting parallel G4s.

1. Introduction

G-quadruplexes (G4s) can be classified as parallel, antiparallel, or hybrid types depending on the topologies arising from their dynamic conformations.[1] Among them, parallel G4s are generally present in several oncogene promoter regions, including *c-MYC*, *VEGF*, and *KRAS*, forming intramolecular parallel G4s.[2,3] Considering their biological significance (*e.g.*, in cell proliferation; their transcription factor regulatory activities; and their natural existence in genomes), intramolecular G4s have been investigated more extensively under specific conditions[4,5] than have been corresponding intermolecular G4s. Various fluorescent probes have been designed for the selective recognition of G4s over duplex [double-stranded (ds)] and single-stranded (ss) DNAs, with some of them functioning under *in vitro* conditions.[6]

Nevertheless, only a few papers have reported topology-oriented selectivities (discrimination between parallel and antiparallel/hybrid topologies) using *in vitro* models.[7] Interestingly, a limited number of such probes have displayed topology-specific variations in their optical properties under physiological conditions.[8] More commonly, the sensing strategies have relied on conjugating G4-stabilizing ligands to conventional fluorophores[9,10] or attaching quencher-free probes (*e.g.*, squarylium,[11,12] thiazolium,[13,14] and pyridinium[15,16] units), accompanied by electron donating or withdrawing groups in both symmetrical and unsymmetrical arrangements, to induce effective push/pull effects. Considering the diverse topologies of G4 structures, various coumarin/anthracene, naphthalene diimide, and squaraine-based fluorescent materials have been developed recently to recognize parallel G4s *in vitro*.[17,19]

Although many fluorescent probes have been reported for the recognition of G4s, the structural similarity between parallel and antiparallel/hybrid topologies has made the development of probes targeting only parallel G4s still challenging, especially in the far-red window.

Based on the concept of conventional aggregation-induced quenching, and considering the variety of homo-supramolecular assemblies

* Corresponding author.
E-mail address: yseo@jbnu.ac.kr (Y.J. Seo).

https://doi.org/10.1016/j.bmc.2021.116077
Received 1 January 2021; Received in revised form 4 February 2021; Accepted 9 February 2021
Available online 16 February 2021

that are typically formed under physiological conditions through cooperative binding between monomer units, we designed probe **1** featuring dual functionalities (phenolic OH and NEt_2 units as electron donors; a pyridinium core as an electron acceptor) to undergo a shift from an intramolecular mode of charge transfer to an intermolecular charge transfer process upon aggregation. Upon consideration of the conformations of the sugar and nucleobase units in each part of the G4 tetrad, especially those in the loop portion, which generally discriminate the parallel and antiparallel G4 topology, we designed our molecular materials (Scheme 1 probes **1**–**4**) to have bent(crescent)/linear shapes, moderate flexibility, and various degrees of hydrophobicity. We validated the sensing capabilities of probe **1** through studies using UV–Vis spectroscopy, fluorescence spectroscopy, ^{1}H NMR spectroscopy, and molecular dynamics (MD)–based simulations.

2. Results and discussion

Probes **1** and **2** were synthesized from lutidine and 2-methylpyridine scaffolds, respectively, by forming their respective 2,6-dimethylpyridinium and 2-methylpyridinium salts and then performing simple Knoevenagel condensations with *N,N*-diethylaminosalicylaldehyde in the presence of a catalytic amount piperidine. Probe **3** was synthesized through the condensation of 4-picolylamine and 1,8-naphthalic anhydride in EtOH and subsequent reaction with 9,10-dicholoromethylanthracene in MeCN. Similarly, probe **4** was prepared from the reaction of quinoline with 9,10-dicholoromethylanthracene. The synthesized probes were characterized using NMR spectroscopy and mass spectrometry (see the ESI).

Photophysical studies of probe **1** in various solvents revealed that it displayed environment-dependent absorption band. Monomer band were exhibited near 510 nm in organic solvent and this band were decreased in the H_2O or H_2O with KCl (aggregation state) (Fig S1a). Fluorescence spectra exhibited monomer emission near 615 nm in organic solvent and this emission were decreased and new band were increased at 730 nm in H_2O or H_2O with KCl; we assumed that this is related with aggregation-induced exciplex emission (Fig S1b, Table ES1).

We examined the aggregation properties of probe **1** in H_2O because we will use this for probe the G-quadruplex structure in buffer condition. Upon addition of various volume-percentages of H_2O to a 1 μM solution of probe **1** in MeCN, we observed concordant decreases in the molar absorptivity with significant broadening in the range 500–760 nm in the UV–Vis spectra (Fig. S2). Such broadening, due to the formation of colloids, is typical of Mie scattering in solution.[20] In addition, we also measured fluorescence spectra of probe **1** (1 μM) in H_2O with various volume-percentages of MeCN. We, firstly, observed quenching emission near 615 nm (±7.5 nm) and exciplex emission at 730 nm in water (aggregation state) and it exhibited increased monomer emission near 615 nm (±7.5 nm) and decreased exciplex emission near 730 nm with increased ratio of MeCN (Fig. S3). We assume that the quenching in monomer emission in aggregation state may be originated from stacking between the electron-deficient $[Py]^+$ units of probe **1** and the electron-rich phenoxide units of probe **1** in the aggregates (ions pairs) led to a strong intermolecular electron coupling–aided charge transfer phenomenon.

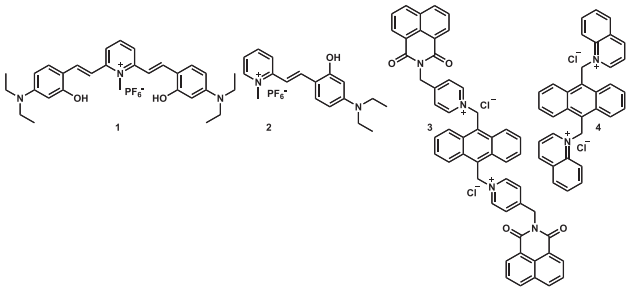

Scheme 1. Structures of our pyridinium (**1**–**3**)- and quinolinium (**4**)-based probes.

Dynamic light scattering (DLS) revealed the formation of molecular aggregates having an average size of 6362.6 nm in H_2O, consistent with our hypothesis (Fig. S4). Excitation-dependent studies revealed shifts in the aggregation-induced exciplex emission wavelength, supporting the presence of nanometer-to-micrometer-sized particles of **1** in H_2O (Fig. S5).

The ground state optimized geometry of **1**, calculated using DFT, revealed that the highest occupied molecular orbitals (HOMOs) and lowest unoccupied molecular orbitals (LUMOs) were distributed in the diethylaminosalicylaldehyde and pyridinium units, respectively, supporting a push/pull-based ICT process. The energy-minimized structure of probe **1** in the ground state geometry had a crescent shape (bent conformation). The obtained band gap energy of –2.42 eV ($\Delta E = E_{HOMO}–E_{LUMO}$) was concordant with the UV–Vis electronic transitions of **1** in H_2O (*ca.* 510 nm). Similarly, the excited state geometry band gap energy ($\Delta E = -2.01$ eV) was in good agreement with the emission maxima at 620 nm (Fig. S6).

Having investigated the photophysical properties of our probe **1** in organic and aqueous conditions and considering the significance of push/pull systems having a bent molecular architecture[21], we used optical methods to examine the interactions of **1** with ODNs having various canonical and non-canonical structure–forming sequences under physiological conditions (Table 1).

UV–Vis spectra of the probe **1** in the presence of 2.0 eq. of parallel G4-forming ODN sequences [*e.g.*, c-MYC (Pu27/22 nt), c-KIT-1, c-KIT-2] featured a sharp monomer band near 510 nm with complete disappearance of the aggregation (broad) band, suggesting efficient disassembly of **1** and the formation of a highly stable complex with a specific molecular confinement (Fig. 1a, b and Fig. S7). Notably, the unfolded versions of the G4-forming ODNs c-MYC (pu27) in H_2O and 22AG in H_2O did not induce any significant degrees of monomer band formation, implying that the probe **1** could recognize parallel G4s only in their folded forms, rather than in their linear/unfolded forms. In contrast, the presence of hybrid and antiparallel-forming G4s [*viz.*, 22AG (K^+/Na^+), TBA, HRAS-1, BOM17] led to minor decreases in aggregation (disassembly of colloids), but it did not induce the appearance of the sharp monomer band in the UV–Vis spectra (Fig. 1b). Similarly, the addition of 2.0 eq. of various ODNs, ssDNA, dsDNA, and hairpin and TWJ ODNs did not result in any significant changes in the broad aggregation band (from > 630 to 750 nm) along with monomer region (Fig. 1b). We suspect that the stronger interactions of the probe **1** with the parallel G4s resulted in sharp increases in the intensity of the monomer bands near 507 nm in the UV–Vis absorption spectra. The relative absorbance ratios $A_{507\ nm}/A_{630\ nm}$ for the parallel G4s were sufficiently high to distinguish them from the rest of the nucleic acids under physiological conditions.

To investigate the selectivity of these interactions, we recorded fluorescence spectra of the solutions in buffered H_2O supplemented with 100 mM KCl. Interestingly, among the various G4-forming ODNs, only the parallel G4-forming ODNs [*i.e.*, c-MYC Pu27/c-MYC (22nt), c-KIT-1, c-KIT-2] provided higher selectivities and sensitivities upon interactions with the probe **1** (Fig. 2 and Fig. S8a) through "*switch on*" (>12-fold) responses in the far-red region (*ca.* 620 nm). For the antiparallel G4-forming ODNs and unfolded G4-forming ODNs [c-MYC (pu27) in H_2O, 22AG in H_2O], the fluorescence enhancement was weaker (<2.0-fold) for the emission centered at 620 nm, concordant with the UV–Vis spectral behavior (Fig. S8b). In contrast, DLS studies of probe **1** with parallel ODNs showed aggregates size in up to 600 nm which was ~ 10 times smaller than the probe **1** aggregations itself in similar conditions (Fig. S4). On the other hand antiparallel, hybrid G4s and dsDNA sequences showed relatively larger particle sizes, compared to that of probe **1** aggregations.

Obtained results clearly suggested that, Probe-**1** disaggregation was

Table 1
ODNs used in this study.

ODN	Sequence 5'→ 3'	Topology/structure	Molar extinction coefficient (L mol^{-1} cm^{-1})
c-MYC (Pu 27)	TGGGGAGGGTGGGGAGGGTGGGGAAGG	Intramolecular parallel	279,900
c-MYC (22)	TGAGGGTGGGTAGGGTGGGTAA	Intramolecular parallel	228,700
c-KIT-1	AGGGAGGGCGCTGGGAGGAGGG	Parallel	226,700
c-KIT-2	CCCGGGCGGGCGCGAGGGAGGGGAGG	Parallel	253,400
TBA	GGTTGGTGTGGTTGG	Intramolecular anti-parallel	143,300
22AG (K^+/ Na^+)	AGGGTTAGGGTTAGGGTTAGGG	Intramolecular anti-parallel/hybrid	228,500
ODN-2/G30	GGGGGGGGGGGGGGGGGGGGGGGGGGGGGG	Intramolecular parallel	304,400
HRAS-1	TCGGGTTGCGGGCGCAGGGCACGGGCG	Intramolecular anti-parallel	250,400
BOM17	GGTTAGGTTAGGTTAGG	Anti-parallel	174,600
Hairpin	ACGTGCCACGATTCAACGUGGCACAG	Not specified	249,700
G-Triplex	AGGGTTAGGGT and TAGGGT	Not specified	114,800 & 61,700
TWJ	CGC AAG CGA CAG GAA CCT CGA GGA ATT CAA CCA CCG GAC G GCA GGC TAG GAC GGA TCC CTC GAG GTT CCT GTC GCT TGC G	Not specified	757,800
ssDNA	CCAGTTCGTAGTAACCC	Single-stranded	160,900
dsDNA	GGGTTACTACGAACTGG & CCAGTTCGTAGTAACCC	Double-stranded	167,400 & 160,900
A30	AAAAAAAAAAAAAAAAAAAAAAAAAAAAAA	Not specified	363,400
T30	TTTTTTTTTTTTTTTTTTTTTTTTTTTTTT	Not specified	243,600
C30	CCCCCCCCCCCCCCCCCCCCCCCCCCCCCC	Not specified	216,200

significant in the case of parallel G4s forming ODNs thereby causing strong intramolecular charge transfer as well as restricted C=C rotations resulted significant changes emission intensity. It is worth to mention that, intermolecularly induced (tightly packed aggregates) exciplex peak was disappeared with most of the ODNs, unambiguously supported the **1**•ODNs complex was predominant species, arose from coulombic force of interactions. Such interactions greatly perturbed the tightly packed molecular orientations of aggregates which resulted in disappearance of exciplex peaks in emission spectra (Fig. S9).

We also examined the effect of various biologically relevant cations and anions and miscellaneous molecules with probe **1.** Fluorescence studies with various biologically relevant cations and anions [*i.e.*, Fe^{3+}, Mn^{2+}, Zn^{2+}, Cu^{2+}, PO_4^{3-}, SO_4^{2-}, HSO_4^-, $HP_2O_7^{3-}$ (PPi), Cl^-, OAc^-, OBz^-] and miscellaneous molecules [glycine (Gly), phenylalanine (PhA), lysine (Lys), serine (Srn), proline (Prl), glutamic acid (Glu)] revealed no effects on the fluorescence behavior of Probe **1** in TRIS-HCl–buffered H_2O at pH 7.2 in the presence of 100 mM KCl (Fig. S8b).

We performed UV–Vis spectroscopic titration studies to evaluate the cooperative binding capabilities of the parallel G4 ODNs with the probe **1** (Fig. 3a). Upon addition of aliquots of c-MYC (Pu27, parallel G-quadruplex) from 0 to 5 μM, Mie scattering effects were diminished with concomitant increases in the intensity of the monomer absorption band, supporting disaggregation effects; these effects were invariant after approximately 4.0 μM had been added (Fig. 3b). In contrast, fluorescence titration studies supported a good binding constant (K_a) of 6.75×10^6 M^{-1} (±1.2%) calculated using a non-linear independent binding site model based on fitting Eq.(**1**) using the Levenberg–Marquardt fitting routine (Origin Professional 2020). Similarly, the association constants for c-KIT-1 and c-KIT-2 were 5.1×10^6 and 4.4×10^6 M^{-1}, respectively (Figs. S10 & 11). We also examined the interaction between probe **1** and parallel G4 ODNs using Job's plots method. Job's plots of the probe **1** with the parallel G4–forming ODNs c-MYC and c-KIT-1/c-KIT-2 supported their 1:2 and 1:1 binding stoichiometries, respectively (Fig. 4).

In contrast, fluorescence titration studies of probe **1** with antiparallel and hybrid G4s revealed that relatively higher concentrations of the ODNs were required to attain saturation (maximum intensity near 620 nm) (Fig. S12). The higher complexity in biomolecular interactions and minor differences in binding process (micro-environments) generally results in various types of non-radiative relaxation process. Due to these reasons binding models were fitted in independent site models which generally does not co-relate the emission intensity and binding constants during calculations[22]. The observed association constants were in the order of 10^4 M^{-1} (Table ES2). These results support the notion of the preferential binding capability of **1** toward parallel G4s over other canonical and non-canonical forms of ODNs, even in the presence of an excess concentration.

Next, we recorded ^{1}H NMR spectra of the c-MYC (22 nt) ODN and the probe **1** to examine their interactions. Because the wild-type c-MYC (Pu 27) sequence forms multiple heterogeneous structures, we recorded ^{1}H NMR spectra using the c-MYC (22 nt) ODN, which uniformly forms a propeller-type parallel structure. Considering the similar binding modes of probe **1** with c-MYC (Pu27) and c-MYC (22 nt), as supported by UV–Vis and fluorescence spectral studies in H_2O at pH 7.2 supplemented with 100 mM KCl, we recorded the ^{1}H NMR spectra. Upon increasing the concentration of the probe **1** from 0 to 6 eq., we observed peak broadening when the probe content ranged from 0.5 to 2.0 eq. and, thereafter, the signal intensity (spinning) diminished slightly upon reaching 6.0 eq. We assume that the signal broadening originated from a bound–unbound state of bonding between the probe **1** and the c-MYC (22 nt) ODN. The observed signals decreased sharply until the ratio of **1** to c-MYC (22 nt) reached 2:1, validating the stoichiometry obtained from the Job's plot (Fig. 5b). Intensity decay profiles revealed prominent changes in surface and bottom G tetrads proton upon addition of various concentrations of probe **1** (0–800 μM), revealed stacking was preferred over groove binding (Fig. 5b). In contrast the upon addition of probe **1** imino signals from the guanine residues, especially G7, G9, and G13, were perturbed significantly (shifted up-field) suggesting that there were stacking modes on either side of the loop, but we did not observe any significant changes in chemical shift for the signals of G8, G12, G17, and G21 in the groove (Fig. 5a).

To evaluate the vital interactions between the probe **1** and the various G4 topologies, we performed molecular simulations using parallel, hybrid, and anti-parallel G4s. Considering the preferential binding toward parallel G4s, we selected c-MYC (22 nt) PDBID **2L7V** for analysis. To validate the behavior of hybrid and anti-parallel G4s, we selected PDBID **2MB3** and 22AG PDBID **143D** for simulation studies. We used molecular docking to identify the possible binding modes (poses) and interaction sites. In addition to the obtained binding poses, we validated the stabilities through MD-based simulations by calculating the binding free energies based on MM/PBSA protocols.

Accordingly, molecular docking studies and trajectory based visualization of the G4:probe **1** complexes in both 1:1 (each at 5' and 3' ends) and 1:2 (5' and 3' ends) stoichiometric relations revealed the two preferential binding sites for the parallel G4–forming c-MYC (22 nt)

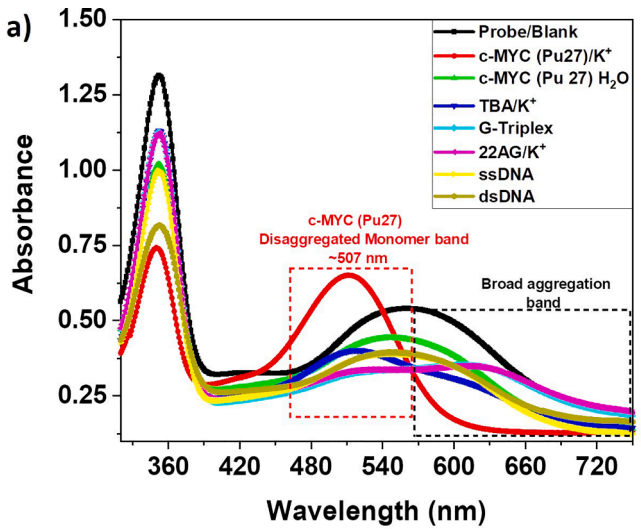

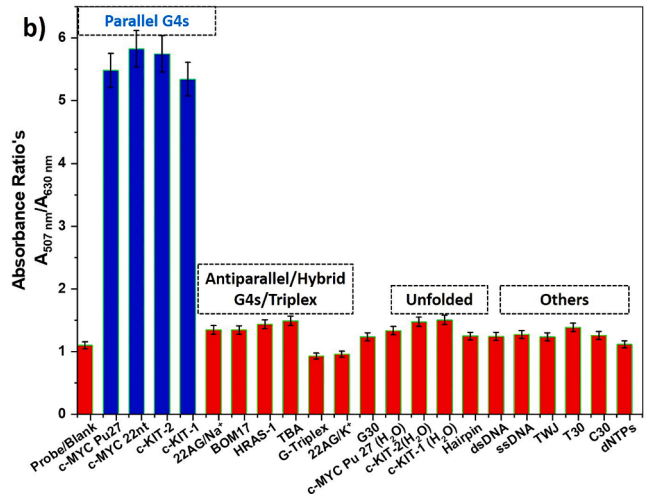

Figure 1. (a) UV–Vis spectra of probe **1** (2 μM) in the absence and presence of various G4s and non-G4s forming ODNs in TRIS-HCl–buffered H_2O at pH 7.2 supplemented with 100 mM KCl. (b) Probe **1** (2 μM) absorbance ratios ($A_{507\ nm}$/$A_{630\ nm}$) measured in the absence and presence of various ODNs or miscellaneous biomolecules. Note: The ODN 22AG was supplemented with 100 mM NaCl to form hybrid G4s. Wherever "H_2O" is specified, only the buffered medium was maintained to examine the interactions of **1** with the unfolded G4-forming ODNs. Errors: <±1.25%.

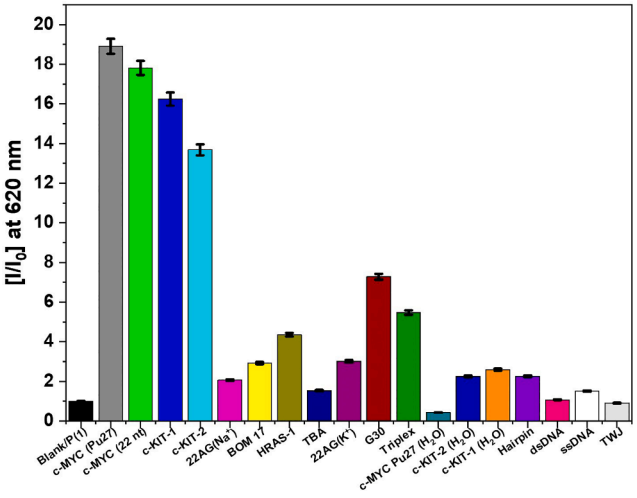

Figure 2. Histogram of relative fluorescence enhancement of probe **1** (1 μM) at λ_{em} 620 nm, in the presence of various canonical and non-canonical ODNs in H_2O (TRIS-HCl, pH 7.2) in the presence of 100 mM KCl/NaCl upon excitation at λ_{ex} = 490 nm. Where I and I_0 are the intensity of the probe **1** at λ_{em} 620 nm, in the presence and absence of analytes. Error<±2.17%

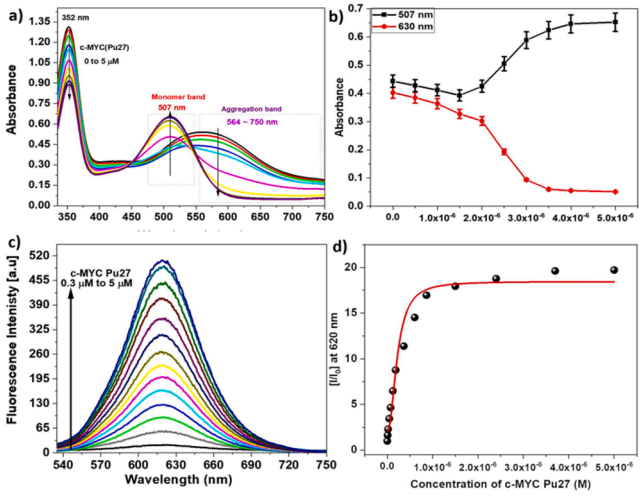

Figure 3. (a) UV–Vis spectra of probe **1** (2.0 μM) in the presence of 0–5 μM c-MYC (Pu27). (b) Absorbance of probe **1** plotted with respect to the concentration of c-MYC (Pu27). (c, d) Fluorescence spectral titration of probe **1** (1 μM) with the c-MYC (Pu27) ODN (0–5 μM) in TRIS-HCl–buffered H_2O at pH 7.2 supplemented with 100 mM KCl. Note: UV–Vis and fluorescence spectral titrations were performed from 0 to 5 μM to minimize errors in fitting the titration data of c-MYC (Pu27) (irregular pattern observed from 0 to 0.3 μM); data taken from 0.3 to 5 μM (saturation point) are presented in the figure.

(PDBID **2L7V**) without changing the quartet structure of the G4 (Fig. 6 and Fig. S13). This finding implies that probe **1** interacted through the end stacking mode with c-MYC (22 nt). The substituents across the styryl units in probe **1** remained in a trans mode; flipping was not observed. Both the 5' end and 3' end docking studies revealed the end stacking mode of the entire surface of probe **1**. The calculated binding free energy component for last 50 ns of the G4:probe **1** (1:2) complex was –2048.735 kJ mol^{-1} (Table ES3); this value is two times higher than that of single ligand interactions, supporting the notion that two-ligand interactions were thermodynamically more feasible.[23] Probe-**1** binding process and its stabilities were monitored RMSD (root mean square deviations) values for the 1:2 G4:probe **1** complex converges through equilibration (i.e high stability) also individual nucleotide contributions revealed that the surface and bottom quartet nucleotides and the loop nucleotides interacted more effectively without harnessing the spurious secondary structure (Fig. S14).

In contrast, the hybrid G4 (PDBID **2 MB3**) underwent groove binding as well as 5' end stacking (Figs. 7a and 7b), but only one mode of binding was stable (either groove binding or 5' end stacking). The groove binding mode (binding free energy: –1180.107 kJ mol^{-1}) was less feasible than the 5' end stacking (binding energy: –1231.429 kJ mol^{-1}). The contributions of the individual nucleotides in pose 1 (groove binding mode) and pose 2 (5' end stacking mode) also revealed that the groove and loop nucleotides were involved in binding process (Figs. S15 & S16).

The antiparallel G4–forming 22AG (PDBID **143D**) also had one-ligand interactions with four different modes of binding (Figs. 7c–f). Among them, pose 3 was relatively unstable (Fig. 7e); it was omitted in from the binding free energy calculations. According to those calculations, pose 1 (groove binding), pose 2 (3' end stacking), and pose 4 (5' end stacking) had free binding energies of –939.008, –926.698, and –874.11 kJ mol^{-1}, respectively. These binding energies are all lower than those of the parallel and hybrid G4 topologies (Table ES3). The

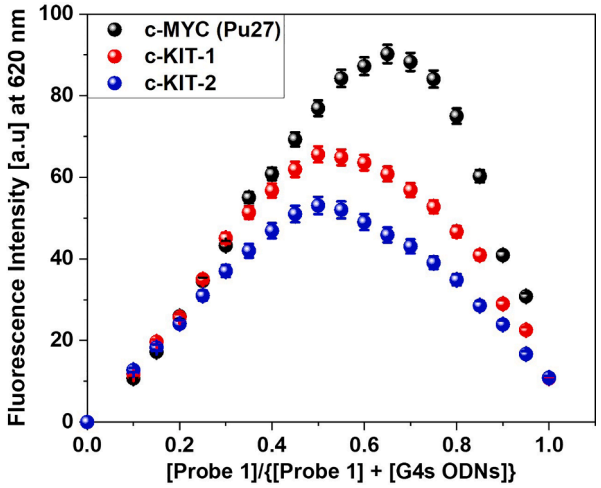

Figure 4. Job's plots of probe **1** (1 μM) and c-MYC (Pu27, 1 μM), c-KIT-1 (1 μM), and c-KIT-2 (1 μM) at pH 7.2 (TRIS-HCl) in the presence of 100 mM KCl. Note: λ_{ex} = 490 nm; λ_{em} = 620 nm. Errors: <±3.55%.

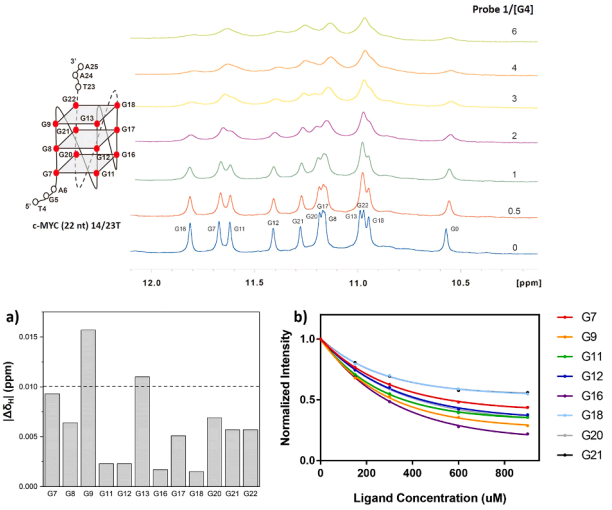

Figure 5. (Top) ^{1}H NMR spectra (Bruker Avance II 700 MHz, equipped with a cryogenic probe; 298 K) of 0.3 mM c-MYC (22nt) recorded in the presence of various concentrations of probe **1** in D_2O at pH 7.2 (20 mM TRIS-HCl) supplemented with 100 mM KCl (1% DMSO). (a) Values of Δδ for various signals from the c-MYC (22 nt) ODN; the dashed line indicates an average + 1 standard deviation; $\Delta\delta = \delta_H$ at [probe **1**/G4] = 1 –δ_H of free G4s; G8, G17, G13, and G22 have been excluded from analysis because of signal overlap. (b) Normalized intensity upon increasing the concentration of probe **1** (0–800 μM).

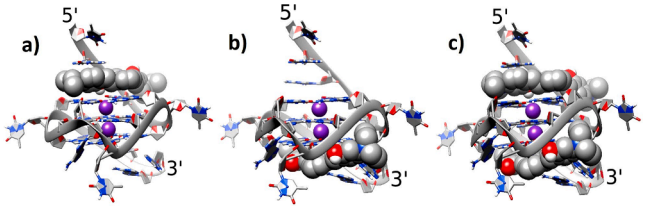

Figure 6. (a, b) Docking studies of probe **1** to the parallel G4–forming c-MYC 22 nt (PDBID **2L7V**) revealing two bindings modes (poses): (a) 2L7V-Pose 1: stacked at 5' end (probe **1** is depicted in a sphere (space-filling) representation; DNA with ribbon backbones and filled base and sugar rings), (b) 2L7V-Pose 2: stacked at 3' end (Pose 2). (c) Probe **1**:DNA modeled in a 2:1 stoichiometry (2L7V-Pose3) for MD simulations.

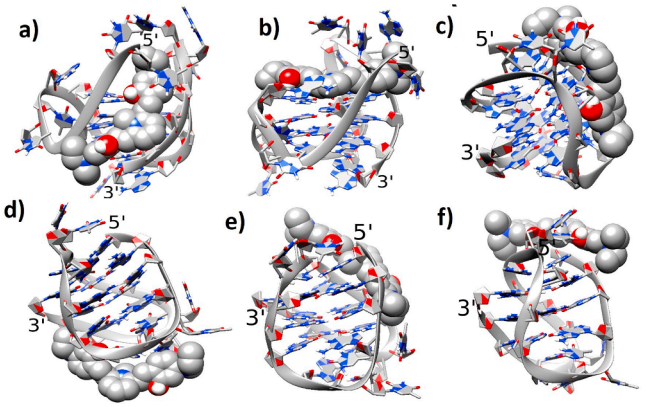

Figure 7. (a, b) Docking of probe **1** to 2 MB3, revealing two bindings poses: (a) 2 MB3-Pose 1: Groove binding; (b) 2 MB3-Pose 2: stacked at 5' end. (c–f) Docking of probe **1** to 143D, revealing four binding poses: (c) Pose 1: groove binding; (d) Pose 2: 3' end stacking; (e) Pose 3: groove binding; and (f) Pose 4: 5' end stacking.

individual nucleotide contributions in poses 1, 2, and 4 of the probe **1**: antiparallel G4 complex revealed that these interactions were hindered because of the sterically crowded environment arising from the diagonal and lateral loops (Figs. S17, S18 & S19).

Based on the optical, NMR spectroscopic, and MD simulation studies, we speculate that the presence of lateral loops on the periphery led to relatively sterically less crowded surfaces of the G4 tetrads on either side (top and bottom) of the parallel G4s, resulting in highly stable (probe **1**)$_2$•G4 complexes.[24,25] This arrangement would lead to the appearance of a perfect monomer emission centered near 620 nm. In antiparallel and hybrid G4s, however, the loops were oriented toward the upper and lower sides of the tetrad, providing additional steric bulk that resulted in weaker π-stacking and, therefore, less stable (probe-**1**)$_2$•G4 complexes.[26–28] The presence of crescent-shaped and flat molecular architectures and the formation of highly stable ions pairs of **1** in the H_2O medium, additionally supported by peripheral NEt_2 substitutions, tended to enhance the selectivity by enhancing conventional noncovalent interactions (*i.e.*, π -stacking, multiple hydrogen bonding, and coulombic interactions).

To validate our hypothesis of molecular geometry–oriented probe•G4 interactions, we examined the behavior of the single-armed probe **2** featuring only one styryl unit. The UV–Vis spectra of the probe **2** featured its value of λ_{max} at 468 nm, without any broadening in the presence of KCl, even at 100 mM, unlike the broadening observed for probe **1** (Fig. S20a) with very low emission behavior in H_2O (Fig. S20b). This finding suggests that greater hydrophilicity tends to enhance the solubility, thereby forming smaller colloids. We examined the interaction of probe **2** with different ODN and different types of G4 sequences. We didn't observed significant changes in absorption spectra and also we could not discriminate the parallel G-quadruplex sequences from other sequences using fluorescence spectra (Fig. S21a, Fig S21b, Fig. S22). The resulting association constants for probe **2** toward the G4s, obtained through fluorescence spectral titration, were on the order of 10^4 to 10^5 M^{-1} (Fig. S23). We speculate that the smaller size of probe **2** meant that it could bind parallel, antiparallel, and hybrid G4s without inducing steric hindrance on either side (top and bottom) of the G4s.[29]

To evaluate the significance of the styryl and pyridinium units, we examined probe **3**, which features a more flexible molecular geometry and greater hydrophobicity, for its opto-analytical capabilities under similar conditions. Considering the significance of π-stacking on a G tetrad (top and bottom sides of the G4s), we incorporated a hydrophobic anthracene moiety at the 4-position of each pyridinium unit to enhance the probability of stacking. In addition, to ensure greater flexibility, we positioned alkyl groups on either side of the anthracene moiety in a symmetrical manner (at the 9- and 10-positions). With such a design, we

expected two different types of π-stacking could occur upon interacting with G4s. Probe **3** did not, however, exhibit any selective discrimination of dsDNA over G4s at pH 7.2 (TRIS-HCl) supplemented with 100 mM KCl in either UV–Vis or fluorescence spectral studies (Fig. S24). The presence of the pyridinium core and the freely rotatable CH_2 groups at the 9- and 10-positions of the anthracene moiety may tend to increase the flexibility and the hydrophobicity, both of which did not favor selective interactions with the G4s. Furthermore, the symmetric zigzag arrangement of the naphthalimide units, resulting from the two freely rotatable methyl groups, on either side of the axially dispersed π-clouds (anthracene core) enhanced the steric hindrance (Fig. S25).

To evaluate the effect of the pyridinium units, we incorporated quinolinium moieties in probe **4** and monitored its opto-analytical capabilities. Again, probe **4** did not display any selectivity toward nucleic acids when tested under conditions similar to those used for probe **1** (Fig. S26). The greater hydrophobicity and rigidity of probe **4** presumably resulted in an imbalance among the coulombic and other non-covalent interactions, leading to inadequate space for probe–ODN interactions and, therefore, the photophysical properties were invariant when interacting with the various nucleic acids under the test conditions.

CD Spectra and Melting Temperatures

We did not observe any significant changes in the CD spectra of the parallel G4–forming sequences [*i.e.*, c-MYC (pu27)[51], c-KIT-1, c-KIT-2] or the antiparallel and hybrid sequences in the absence and presence of the probe **1** (Fig. S27). Nevertheless, the CD spectra in the 400–700 nm region in the absence and presence of **1** revealed that the helicity changed in the region near 500 nm (Figs.S27a–d).Furthermore, the normalized melting temperatures, measured using the absorbance at 295 nm, revealed a slight increase in the values of T_m (2.2–2.8 °C) when the probe **1** interacted with the parallel G4s; we did not observe such changes when **1** interacted with the antiparallel G4s. Thus, the probe **1** appears to not significantly stabilize the secondary structures on the surfaces of the parallel G4s (Fig. S28, Table ES4).

The crescent shape and flat molecular configuration of probe **1** can lead to highly stable ion pair–based aggregates in buffered H_2O, additionally stabilized by 100 mM KCl because of common ion effects in aqueous media. Those aggregates dissolved specifically (disaggregated) only in the presence of parallel G4–forming ODNs, giving clear solutions. The high selectivity and sensitivity of probe **1** toward the c-MYC (Pu27) ODN presumably arose because the four flanking guanine residues on the 5' end and the purine bases (AAGG) on the 3' end could further stabilize the hydrophobic interior of the G4s through additional π-stacking interactions.[30,31] For the antiparallel and hybrid G4s, however, the lateral, diagonal, and v-shaped loops tended to increase the steric hinderance when stacked on either side of the G4 tetrads (MD studies).

From the results obtained from the ^{1}H NMR spectral studies, we suspect that the guanine residues on the top and bottom sides of the c-MYC (22 nt) G4s were significantly perturbed, because those tetrads were open for ligand interactions without any steric factors. Accordingly, the signals of the G7, G9, G13, and G20 nucleobases underwent significant changes upon interacting with probe **1**. The presence of pyrimidine units in the loops, as well as in the flanking ends, typically leads to less steric hindrance than does the presence of larger purine residues (near to top and bottom tetrads of the G4s); for this reason, the changes in chemical shift were not similar on the two sides of the tetrads.[32,33] Additionally, MD studies also supported our hypothesis that parallel G4s typically form more stable conformations, due to propeller loops, without harnessing any spurious secondary structure.

Based on these results, we believe that the parallel G4s (c-MYC, c-KIT-1, c-KIT-2) typically feature propeller loops in a regular or unusual mode (sometimes acting as lateral loops). Such orientations result in more flexible conformations in the loop, tending to enhance the surface/bottom stacking mode very effectively. Thus, we believe that the disaggregation of **1** was very effective in the presence of parallel G4-forming ODNs, due to the presence of highly available free surface area, resulting in more highly negative values for the change in free energy (ΔG) of formation upon complexation (Fig. 8).

In contrast the model compounds such as **2**, **3** and **4** recognition capabilities were varied according to the molecular geometry, hydrophilicity and hydrophobicity's supports the crescent shaped molecular architecture with optimized hydrophobic and hydrophilic properties are essential factors for the discrimination of G4s with various topology (Table ES5). In addition to that, size of the probe **1**, was found appropriately fit to stack on surface and bottom tetrads, helps to inhibit the free rotation of styryl (C═C) units resulted in highly rigid confinements tend to enhance the intramolecular charge transfer process at maximal extent. Due to these reasons, high intensity monomer emission was observed only in the case of parallel G4s (freely available tetrads for π-π stacking), than the conventional groove binding or intercalation mode (Fig. 9). Additionally probe **1** parallel G4s discrimination over antiparallel/hybrid G4s were comparatively significant from recently reported far red emissive molecules.[45–50]

3. Experimental section

3.1. Synthesis of probes

Probe 1: A solution of lutidine (2.00 g, 18.7 mmol) and MeI (2.32 g, 37.3 mmol) in CH_2Cl_2 (50 mL) was stirred under a N_2 atmosphere at room temperature for 5 h, monitoring through TLC. The creamy white solid was filtered off, washed with ether (3 × 15 mL), and dried under vacuum to give *1,2,6-trimethylpyridinium iodide* (89%); ^{1}H NMR [400 MHz, $CDCl_3$, δ (ppm)] 2.97 (s, 6H), 4.03 (s, 3H), 7.74 (d, J = 7.90 Hz, 2H), 8.18 (t, J = 7.90 Hz, 1H); ^{13}C NMR (100 MHz, $CDCl_3$) δ 23.4, 42.6, 128.0, 144.2, 156.1; ESI-MS $[C_8H_{12}N]^+$, m/z 122.10. A mixture of 1,2,6-trimethylpyridinium iodide (2.00 g, 8.03 mmol), 4-(diethylamino)salicylaldehyde (3.49 g, 18.1 mmol), and piperidine (catalytic amount) was heated under reflux in toluene (100 mL) under N_2 in a Dean–Stark apparatus for 16 h, monitoring through TLC. The mixture was concentrated to dryness and the solid residue washed with Et_2O. A mixture of the brownish solid (I^- salt) and KPF_6 (17.2 g, 93.3 mmol) in MeCN (125 mL) was heated under reflux for 14 h and then evaporated to dryness. The dark-pink semisolid was dissolved in CH_2Cl_2 and filtered through a Celite-545 pad. The eluate was further purified through flash column chromatography (SiO_2; EtOAc/CH_2Cl_2/hexane/MeOH, 6:2:1:1) to furnish 1 as a dark-pink amorphous solid (350 mg, 70%); ^{1}H NMR [400 MHz, DMSO-d_6, δ (ppm)] 1.12 (t, J = 6.8 Hz, 12H), 3.37 (q, J = 6.8 Hz, 8H), 4.07 (s, 3H), 6.19 (d, J = 2.4 Hz, 2H), 6.29 (dd, J = 5.2, 2.4 Hz, 2H), 7.22 (d, J = 15.6 Hz, 2H), 7.55 (d, J = 8.8 Hz, 2H), 7.74 (d, J = 15.6 Hz, 2H), 7.90 (d, J = 8.0 Hz, 2H), 8.05 (t, J = 8.0 Hz, 1H), 10.07 (s, 2H); ^{13}C NMR [100 MHz, DMSO-d_6, δ (ppm)] 13.1, 44.4, 97.7, 104.8, 110.7,

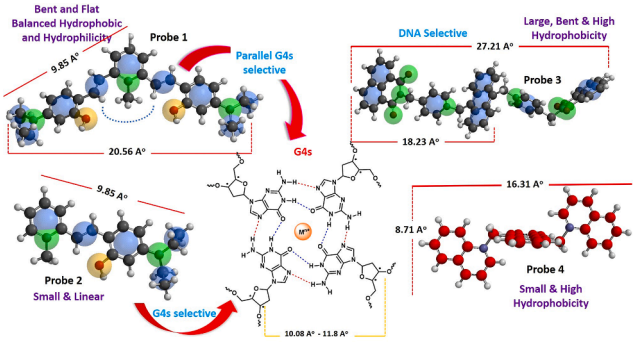

Figure 8. Plausible sensing mechanisms of the pyridinium- and quinolinium-based probes **1**–**4**.

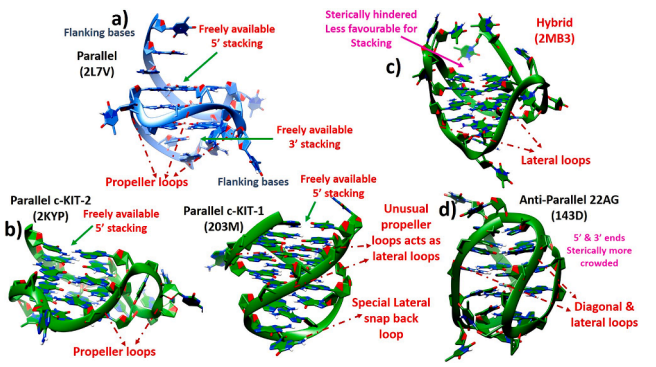

Figure 9. Plausible mode of interactions of probe **1** with various types of G4 ODNs according to their loop orientations (propeller, diagonal, and lateral) in parallel and antiparallel topologies. Respective G4 structures were adopted from the references noted in the Experimental section.

112.0, 120.3, 131.4, 138.6, 141.4, 151.2, 154.6, 159.3; HR-MS: calcd for $[C_{30}H_{38}N_3O_2]^+$ $[M]^+$ *m/z* 472.2964, found 472.2961.

Probe ***2***: A solution of 2-methylpyridine (2.00 g, 21.5 mmol) and MeI (2.00 g, 32.2 mmol) was stirred in dry CH_2Cl_2 (50 mL) under a N_2 atmosphere at room temperature. Upon completion of the reaction (TLC), the mixture was evaporated to dryness. The solid residue was washed thoroughly with cold EtOAc/Et_2O (2:8, v/v) several times and then dried under high vacuum to furnish *2-methyl-N-methylpyridinium iodide* (2a) as a creamy white solid (94%); ^{1}H NMR [400 MHz, DMSO-d_6, δ (ppm)] 2.80 (s, 3H), 4.25 (s, 3H), 7.96 (t, J = 6.8 Hz, 1H), 8.06 (d, J = 8.0 Hz, 1H), 8.48 (t, J = 7.6 Hz, 1H), 9.00 (d, J = 6.0 Hz, 1H); ^{13}C NMR [100 MHz, DMSO-d_6, δ (ppm)] 20.5, 46.0, 125.7, 129.6, 145.4, 146.5, 156.4; ESI-MS$^+$: *m/z* 108.20. A solution of 2a (0.500 g, 4.62 mmol), 4-(diethylamino)salicylaldehyde (0.940 g, 4.85 mmol), and piperidine (catalytic amount) in dry toluene (50 mL) was heated under reflux under N_2 in a Dean–Stark apparatus for 16 h. Upon completion of the reaction (TLC), the solvent was evaporated to dryness. The dark-red powdery residue and KPF_6 (2.13 g, 11.6 mmol) were dissolved in ethylene dichloride (50 mL) and heated under reflux under N_2 for 12 h. The mixture was filtered through a pad of Celite 545 and evaporated. The dark-pink powdery residue was purified through flash silica column chromatography (SiO_2; EtOAc/CH_2Cl_2/hexane/MeOH, 6:1:2:1) to furnish **2** as a dark-red solid (60%); ^{1}H NMR [400 MHz, DMSO-d_6, δ (ppm)] 1.13 (t, J = 6.99 Hz, 6H), 3.38 (q, J = 7.00 Hz, 4), 4.20 (s, 3H), 6.20 (d, J = 2.33 Hz, 1H), 6.33 (dd, J = 8.97, 2.32 Hz, 1H), 7.22 (d, J = 15.65 Hz, 1H), 7.59 (d, J = 8.80 Hz, 2H), 7.97 (d, J = 16.65 Hz, 1H), 8.24 (d, J = 15.72 Hz, 1H), 8.35 (d, J = 8.22 Hz, 1H), 8.68 (d, J = 6.15 Hz, 1H), 10.23 (s, 1H); ^{13}C NMR [100 MHz, DMSO-d_6, δ (ppm)] 13.1, 44.2, 44.5, 45.8, 97.5, 105.0, 109.4, 110.7, 122.4, 123.4, 132.1, 140.5, 143.1, 145.4, 151.8, 154.4, 159.9; HR-MS: calcd for $[C_{18}H_{23}N_2O]^+$ $[M]^+$ *m/z* 283.1810, found 283.1808.

Probe ***3***: A solution of 1,8-naphthalic anhydride (2.00 g, 10.1 mmol) and 4-(aminomethyl)pyridine (1.18 g, 11.6 mmol) in anhydrous EtOH (50 mL) was heated under reflux for 8 h. Upon completion of the reaction (TLC), the mixture was cooled to room temperature and left for 10 h to furnish creamy-white needle-shaped crystals, which were washed with EtOH/H_2O (2:8) at 10 °C and dried under vacuum to give 2-(4-pyridylmethyl)-1*H*-benz[*de*]isoquinoline-1,3(2*H*)-dione (3a, 88%). ^{1}H NMR [400 MHz, $CDCl_3$, δ (ppm)] 5.31 (s, 2H), 7.31 (dd, J = 1.2, 3.2 Hz, 2H), 7.69–7.73 (m, 2H), 8.18 (dd, J = 7.6, 0.8 Hz, 2H), 8.47 (dd, J = 2.8, 1.6 Hz, 2H), 8.55–8.57 (m, 2H); ^{13}C NMR [100 MHz, $CDCl_3$, δ (ppm)] 42.6, 122.3, 123.3, 127.1, 128.3, 131.7(d), 134.5, 145.9, 150.0, 164.2; API$^+$-MS $[C_{18}H_{12}N_2O_2 + H]^+$, *m/z* 289.18. A mixture of 3a (2.00 g, 6.94 mmol) and 9,10-bisdichloromethylanthracene[44] (0.960 g, 3.47 mmol) in dry MeCN was heated under reflux under N_2 for 14 h. Upon completion of the reaction (TLC), the solvent was evaporated to dryness. The solid residue was dissolved in THF/EDC/MeOH (2:3:5) and subjected to slow evaporation under N_2 at room temperature. The crystals that formed were collected through filtration to furnish **3** as a yellowish powder (50%); ^{1}H NMR [400 MHz, DMSO-d_6, δ (ppm)] 5.47 (s, 4H), 7.03 (s, 4H), 7.74–7.76 (m, 4H), 7.91 (t, J = 7.6 Hz, 5H), 8.07 (d, J = 6.4 Hz, 4H), 8.49 (d, J = 7.2 Hz, 4H), 8.54–8.57 (m, 7H), 8.76 (d, J = 6.4 Hz, 4H); ^{13}C NMR [100 MHz, DMSO-d_6, δ (ppm)] 47.9, 60.2, 127.2, 128.9, 129.9, 131.0, 131.2, 131.4, 132.5, 133.0, 133.4, 134.9, 136.2, 136.6, 140.1, 148.9, 149.1, 162.8, 168.9; HR-FAB MS: calcd for $\{[C_{52}H_{36}N_4O_4] + Cl^-\}^+$, *m/z* 815.2427, found 815.2427.

Probe ***4***: A solution of 9,10-bisdichloromethylanthracene (2.00 g, 7.27 mmol) and quinoline (2.15 g, 18.2 mmol) in MeCN was heated under reflux under N_2 for 12 h. The mixture was concentrated under vacuum and then the solid residue dissolved in THF/EtOAc (6:4, v/v). The solution was filtered through a pad of Celite 545 and then evaporated to dryness. The solid residue was washed with cold THF/Et_2O (7:3, v/v) to furnish **4** as a dark-yellow powder (56%). ^{1}H NMR [400 MHz, DMSO-d_6, δ (ppm)] δ 7.36 (s, 4H), 7.67 (dd, J = 8.0, 2.8 Hz, 4H), 7.87–7.90 (m, 2H), 8.23–8.26 (m, 2H), 8.47 (dd, J = 8.0, 2.4 Hz, 4H), 8.54 (dt, J = 7.2, 1.2 Hz, 2H), 8.65 (d, J = 5.6 Hz, 4H), 9.29 (d, J = 7.2 Hz, 2H), 9.35 (d, J = 6.8 Hz, 2H); ^{13}C NMR [100 MHz, DMSO-d_6, δ (ppm)] 53.3, 120.5, 122.8, 125.3, 125.6, 128.7, 130.4, 130.8, 131.1, 132.4, 136.1, 139.6, 147.2, 148.2; HR-FAB MS: calcd for $\{[C_{34}H_{26}N_2] + Cl^-\}^+$, *m/z* 497.1785, found 497.1783.

3.2. Computational studies

Density functional theory (DFT)-based molecular simulations were performed according to previously reported procedures.[34] Energy-minimized structures of the probes were determined in H_2O as an implicit medium (SM8 model). The xyz coordinates of the thus-obtained DFT-based geometries were used for molecular docking studies and subsequent MD studies with G4 structures.

Molecular modeling and MD simulations were performed initially with G4s of various topologies, retrieved from the Protein Data Bank (PDB) ID source: c-MYC (22 nt, Parallel) PDB ID 2L7V,[35] PDB ID 2 MB3 (hybrid),[36] and 22AG (antiparallel) PDB ID 143D.[37] To identify the binding sites and conformations of the ligands to the G4s, various topological molecular docking studies were performed using Autodoc 4.2 by choosing a sufficiently large grid box to cover the whole G4.[38] The Lamarckian genetic algorithm was used for docking with 250,000 energy evaluations from an initial population of 150 randomly placed individuals having a mutation rate of 0.02 along with a maximum number of 27,000 generations. A crossover rate of 0.8 and 300 iterations of local search were used. Finally, 10 independent docking runs were performed for each G4 topology.

Further, MD simulations were performed for the modeled G4-ligand complexes through all-atom MD simulations using the GROMACS-2018.6 package.[39] The force field parameters and atomic charges for the ligands were derived from the generalized AMBER force field2 (GAFF2) and bcc charges using the ANTECHAMBER module of the AMBERTOOLS20 package.[40] Topologies for DNA were generated from AMBER99SB-ILDN force field. The modeled complex was placed in the triclinic box with a minimum distance of 1.2 nm from the box edges under the periodic boundary conditions. The solvent was filled using the TIP3P water model and the total system was neutralized by replacing Na^+ and Cl^- with solvent molecules. Next, energy minimization was performed for 50,000 steps using the steepest descent algorithm with the energy tolerance of 1000 kJ mol^{-1} nm^{-1}. NVT (number of volume temperature) and NPT (number of pressure temperature) equilibration simulations of 2 ns were performed by restraining the DNA-ligand complex to attain a temperature and pressure of the simulated system of 300 K and 1 bar, respectively, using v-rescale and the Parinello-Rahman barostat. Finally, 50-ns production simulations were performed using the NPT ensemble. Long-range interactions were handled using the particle mesh Ewald (PME) method. Hydrogen bonds were constrained with the LINCS algorithm. Binding energy calculations were

performed using the g mmpbsa module.[41] All analyses were performed using built-in GROMACS tools. Visualizations and image rendering were performed using visual molecular dynamics (VMD)[42] and Chimera[43] packages. Gnuplot was used for drawing graphs.

4. Conclusion

We have demonstrated that probe **1**, a simple pyridinium-based salt, allows the identification of parallel G4s over antiparallel and hybrid G4 topologies as well as other non-canonical/canonical forms of DNA (*i.e.*, ssDNA, dsDNA, Poly G, triplex, TWJ). Probe **1** recognized the tested parallel G4s with a selective *switch on* response in the far-red emission region, with excellent selectivity and sensitivity. We analyzed the selective sensing capabilities of probe **1** using UV–Vis spectroscopy, fluorescence spectroscopy, ^{1}H NMR spectroscopy, and molecular dynamics (MD)–based simulation studies. We confirm that the disaggregation of probe **1** was very effective in the presence of parallel G4–forming ODNs, due to the presence of highly available free surface area, resulting in additional π-stacking interactions. In addition, we have postulated our hypothesis based on systematic analysis of various model compounds 2, **3** and **4** by changing, molecular geometry, hydrophilicity and hydrophobicity under similar experimental conditions. Thus, simple molecules and cost-effective strategies can be used to identify G4s with appreciably good topological selectivity. Studying rationally designed probes appears to be excellent initial platform for designing novel G4-tracking functional materials and their therapeutics.

Declaration of Competing Interest

The authors declare that they have no known competing financial interests or personal relationships that could have appeared to influence the work reported in this paper.

Acknowledgement

This study was supported by the Basic Science Research Program through the National Research Foundation of Korea (2017R1A2B4002398), funded by the Republic of Korea.

Appendix A. Supplementary material

Supplementary data to this article can be found online at https://doi.org/10.1016/j.bmc.2021.116077.

References

1 Yang D, Okamoto K. *Future Med Chem*. 2010;2:619–646.
2 Manna S, Srivatsan SG. *RSC Adv*. 2018;8:25673–25694.
3 Largy E, Granzhan A, Hamon F, Verga D. *Top Curr Chem*. 2013;330:111–177.
4 Konig SLB, Evans AC, Huppert JL. *BioMol Concepts*. 2010;1:197–213.
5 Murat P, Balasubramanian S. *Curr Opin Gen Dev*. 2014;25:22–29.
6 Suseela Y, Narayanaswamy V, Pratihar S, Govindaraju T. *Chem Soc Rev*. 2018;47:1098–1131.
7 Yuan JH, Shao W, Chen S-B, Huang Z-S, Tan J-H. *Biochem Biophys Res Commun*. 2020;531:18–24.
8 Pandith A, Siddappa RG, Seo YJ. *J Photochem Photobiol C: Rev*. 2019;40:81–116.
9 Vummidi BR, Alzeer J, Luedtke NW. *ChemBioChem*. 2013;14:540–558.
10 Ma D-L, Zhang Z, Wang M, Lu L, Zhong H-J, Leung C-H. *Chem Biol*. 2015;22:812–828.
11 Grande V, Shen C-A, Deiana M, et al. *Chem Sci*. 2018;9:8375–8381.
12 Zhang X, Wei Y, Bing T, et al. *Sci Rep*. 2017;7:4766.
13 Zhang S, Sun H, Wang L, et al. *Nucleic Acids Res*. 2018;46:7522–7532.
14 Chen Y, Yan S, Yuan L, et al. *Org Chem Front*. 2014;1:267–270.
15 Tseng T-Y, Wang Z-F, Chien C-H, Chang T-C. *Nucleic Acids Res*. 2013;41:10605–10618.
16 Huang W-C, Tseng T-Y, Chen Y-T, et al. *Nucleic Acids Res*. 2015;43:10102–10113.
17 He H-Z, Chan D-S-H, Leung C-H, Ma D-L. *Nucleic Acids Res*. 2013;41:4345–4359.
18 Kumar R, Chand K, Bhowmik S, et al. *Nucleic Acids Res*. 2020;48:1108–1119.
19 Yang C, Hu R, Li Q, et al. *ACS Omega*. 2018;3:10487–10492.
20 Horn D, Rieger J. *Angew Chem Intl Ed*. 2001;40:4330–4361.
21 Klikar M, Solanke P, Tydlitát J, Bureš F. *The Chemical Record*. 2016;16:1886–1905.
22 Jin B, Zhang X, Zheng W, et al. *Anal Chem*. 2014;86:943–952.
23 Chen S-B, Wu W-B, Hu M-H, et al. *Chem Commun*. 2014;50:12173–12176.
24 Yang Q, Xiang J, Yang S, et al. *Nucleic Acids Res*. 2010;38:1022–1033.
25 Zhang L, Cheng Er J, Li X, et al. *Chem Commun*. 2015;51:7386–7389.
26 Asamitsu S, Bando T, Sugiyama H. *Chem Eur J*. 2019;25:417–430.
27 Harikrishna S, Kotaru S, Pradeepkumar PI. *Mol BioSyst*. 2017;13:1458–1468.
28 Deiana M, Chand K, Jamroskovic J, Obi I, Chorell E, Sabouri N. *Angew Chem Intl Ed*. 2020;132:906–912.
29 Xie X, Reznichenko O, Chaput L, Martin P, Teulade-Fichou M-P, Granzhan A. *Chem Eur J*. 2018;24:12638–12651.
30 Bhat J, Chatterjee S. *RSC Adv*. 2016;6:36667–36680.
31 Bessi I, Wirmer-Bartoschek J, Dash J, Schwalbe H. *Modern Magnetic Reson*. 2018;13:2189–2210.
32 Le DD, Antonio MD, Chana LKM, Balasubramanian S. *Chem Commun*. 2015;51:8048–8050.
33 Dash J, Shirude PS, Hsu S-T-D, Balasubramanian S. *J Am Chem Soc*. 2018;130:15950–15956.
34 Pandith A, Seo YJ. *J Inorg Biochem*. 2020;203, 110867.
35 Dai J, Carver M, Hurley LH, Yang D. *J Am Chem Soc*. 2011;133:17673–17680.
36 Chung WJ, Heddi B, Tera M, Iida K, Nagasawa K, Phan AT. *J Am Chem Soc*. 2013;135:13495–13501.
37 Wang Y, Patel DJ. *Structure*. 1993;1:263–282.
38 Morris GM, Huey R, Lindstrom W, et al. *J Comput Chem*. 2009;30:2785–2791.
39 Abraham MJ, Murtola T, Schulz R, et al. *SoftwareX*. 2015;1:19–25.
40 Salomon-Ferrer R, Götz AW, Poole D, Le Grand S, Walker RC. *J Chem Theory Comput*. 2013;9:3878–3888.
41 Kumari R, Kumar R, Consortium OSDD, Lynn AJ. *Chem Inform Model*. 2014;54:1951–1962.
42 Humphrey W, Dalke A, Schulten K. *J Mol Graphics*. 1996;14:33–38.
43 Pettersen EF, Goddard TD, Huang CC, et al. *J Comput Chem*. 2004;25:1605–1612.
44 Pandith A, Uddin N, Choi C-H, Kim H-S. *Sens Actuators B*. 2017;247:840–849.
45 Doria F, Nadai M, Zuffo M, Perrone R, Freccero M, Richter SN. *Chem Commun*. 2017;53:2268–2271.
46 Yu L, Yang Q, Xiang J, Tang Y. *Anal Methods*. 2015;7:5483–5489.
47 Zhang F, Li G, Lv F-L, Jian G-B, Wang H-X, Wang M-Q, Li S. *Tet Lett*. 2018;59:3272–3278.
48 You D, Liu L, Yang Q, Wu X, Li S, Li A. *Dyes Pigm*. 2020;176, 108222.
49 Gao F, Cao S, Sun W, Long S, Fan J, Peng X. *Dyes Pigm*. 2019;171, 107749.
50 Wang X-L, Zhang J-T, Sun X, Yang D-W, Tang Y-L. *Dyes Pigm*. 2021;185, 108882.
51 Calabrese DR, Chen C, Leon EC, et al. *Nat Commun*. 2018;9:4229. https://doi.org/10.1038/s41467-018-06315.